Inorg. Chem. **2004**, *43*, 1441−1451

Correlation between the Magnetic g Tensors and the Local Cysteine Geometries for a Series of Reduced [2Fe−2S*] Protein Clusters. A Quantum Chemical Density Functional Theory and Structural Analysis

Serge Gambarelli* and Jean-Marie Mouesca*

Service de Chimie Inorganique et Biologique, Département de Recherche Fondamentale sur la Matière Condensée, CEA−Grenoble, 17 rue des Martyrs, 38041 Grenoble Cedex 9, France

Received March 31, 2003

We relied on the density functional theory (DFT) to study the electronic structure of the [2Fe−2S*](SH)$_4$ model of the active site of 2Fe ferredoxins and other proteins containing reduced [2Fe−2S*] clusters. The two (Fe^{3+}–Fe^{2+}–S–H) dihedral angles Ω_1 and Ω_2 defined for the two ligands on the ferrous side were allowed to vary, while the two other (Fe^{2+}–Fe^{3+}–S–H) angles Ω_3 and Ω_4 on the ferric side were kept constant. The Landé (**g**), magnetic hyperfine, and quadrupole tensors for two geometries, C_2 ($\Omega_1 = \Omega_2$) and C_s ($\Omega_1 = -\Omega_2$), were calculated. To apply our model to the actual proteins, we listed all of the crystallographic structures available for the [2Fe−2S*] systems. A classification of these proteins, based on the four dihedral angles $\{\Omega_i\}_{i=1-4}$, separates them into three main classes. The main structural feature of the first class ($\Omega_1 \approx \Omega_2$), with an average dihedral angle $\Omega_{av} = (\Omega_1 + \Omega_2)/2$ comprised between 115° and 150°, corresponds to a local ferrous C_2 geometry (rather than C_{2v}, as previously assumed by Bertrand and Gayda: *Biochim. Biophys. Acta* **1979**, *579*, 107). We then established a direct correlation between the three principal **g** values and Ω_{av}. It is the first time that such a link has been made between the spectroscopic and structural parameters, a link, moreover, fully rationalized by our DFT calculations. We finally point out the basic differences between our C_2 results with those of the C_{2v} phenomenological model proposed in the late 1970s by Bertrand and Gayda.

Introduction

Iron−sulfur proteins exhibit a great variety of prosthetic groups, the most common ones containing [2Fe−2S*], [3Fe−4S*], or [4Fe−4S*] clusters at their active sites.[1,2] Among the [2Fe−2S*] systems, one can distinguish two major branches depending on the ligands coordinating the iron sites. There are the "Rieske-type" proteins,[3] whose ferrous site is coordinated by two histidines. In the remaining systems, each iron atom is linked to the main amino acid chain through two cysteines. In this configuration, they participate in the protein's function through electron transfer or as part of the catalytic site. We will deal with the non-Rieske-type proteins in the remainder of this study.

[2Fe−2S*] ferredoxins are ubiquitous small electron-transfer proteins found in archaea, plants, and humans, where they serve as one-electron-oxidation or -reduction sites. Most of them belong to the large monophyletic family of plant- and mammalian-type ferredoxins. On the basis of sequencing and 3D data, this family can be divided into two subgroups.[1,4,5]

The first subgroup, plant-type ferredoxins, present in plants and algae are usually about 100 residues long. Some serve in chloroplasts as electron carriers from photosystem I to the ferredoxin/$NADP^+$ reductase (e.g., *Spirulina platensis*[6]

* Authors to whom correspondence should be addressed. E-mail: gambarel@drfmc.ceng.cea.fr (S.G.); mouesca@drfmc.ceng.cea.fr (J.-M.M.).

(1) Johnson, M. K. In *Encyclopedia of Inorganic Chemistry*; King, R. B., Ed.; Wiley: Chichester, England, 1994; Vol. 4, pp 1896−1915.
(2) Sykes, A. G.; Cammack, R. In *Advances in Inorganic Chemistry: Iron−Sulfur Proteins*; Sykes, A. G., Cammack, R., Eds.; Academic Press: London, 1999; Vol. 47.
(3) Link, T. A. In *Advances in Inorganic Chemistry: Iron−Sulfur Proteins*; Sykes, A. G., Cammack, R., Eds.; Academic Press: London, 1999; Vol. 47, p 83.
(4) Holden, H. M.; Jacobson, B. L.; Hurley, J. K.; Tollin, G.; Oh, B. H.; Skjeldahl, L.; Cheng, Y. K.; Xia, B.; Markley, J. L. *J. Bioenerg. Biomembr.* **1994**, *26*, 67−88.
(5) Mitou, G.; Higgins, C.; Wittung-Stafshede, P.; Conover, R. C.; Smith, A. D.; Johnson, M. K.; Gaillard, J.; Stubna, A.; Münck, E.; Meyer, J. *Biochemistry* **2003**, *42*, 1354−1364.
(6) Tsukihara, T.; Fukuyama, K.; Nakamura, M.; Katsube, Y.; Tanaka, N.; Kakudo, M.; Wada, K.; Hase, T.; Matsubara, H. *J. Biochem.* **1981**, *90*, 1763−1773.

10.1021/ic0301167 CCC: $27.50
Published on Web 01/17/2004

and vegetative *Anabaena* 7120). Others are involved in the process of nitrogen fixation, for example, the cyanobacterial ferredoxin of (heterocyst) *Anabaena* 7120. The **g** tensors of these photosynthetic ferredoxins tend to be rhombic (typically 2.05, 1.96, 1.88).[7,8]

The second subgroup comprises mammalian- and bacterial-type ferredoxins, which are longer than the plant-type ferredoxins (~130 residues). The mammalian placental and adrenal (adrenodoxin) ferredoxins are involved in electron transfer from a ferredoxin reductase to cytochrome P450 enzymes in the mitochondria. Examples of bacterial ferredoxins are putidaredoxin from *Pseudomonas putida* and the bacterial isc ("iron−sulfur center assembly") ferredoxins.[9,10] The **g** tensors of the bacterial (putidaredoxin) and mitochondrial (adrenodoxin) ferredoxins tend to be axial (2.02, 1.93, 1.93).[7,8]

In this paper, we will also consider a newly discovered class of systems exhibiting [2Fe−2S*] clusters, e.g., the thioredoxin-like proteins (such as those from *Aquifex aelolicus*),[11,12] which present an unexpected structural similarity to thioredoxin. We will also mention in our analysis the xanthine oxidase type enzymes.[13]

For these [2Fe−2S*] proteins, there exists a *phenomenological* model rationalizing the correlation observed[14] between the three $\{g_i\}$ principal values ($g_{max} > g_{mid} > g_{min}$, with an average value around 1.96) when plotting each g_i as a function of $g_{mid} - g_{min}$ (Bertrand and Gayda's model[7,8]). Because an increasing number of 3D crystal structures for the [2Fe−2S*] systems are becoming available, we can now try to ground this model on a firm experimental (i.e., structural) basis, because there is a growing need to establish a clear correlation between spectroscopic values (readily obtained in frozen solutions: **g** tensors, Mössbauer parameters, etc.) and precise structural features.

From a computational point of view, the application of the density functional theory (DFT) to molecules allowed the calculation of the electronic structures of the transition-metal complexes such as the iron−sulfur clusters.[15−18] The first calculations of the **g**-tensor values for the [2Fe−2S*](SH)$_4$ clusters appeared in 1984.[17] One of the key points of these studies lies in the effect of the orientation of the S−H bond on the relative ordering of the ferrous d orbitals.[7,17,19,20] However, these theoretical studies have been performed with assumed high molecular (C_{2v}) symmetry, i.e., with the four (Fe−Fe−S−H) dihedral angles $\{\Omega_i\}_{i=1-4}$ constrained to either 0° or 180°. Recently, an exhaustive study of the rubredoxins[21] linked precise geometric features with computed spectroscopic quantities [Mössbauer, electron paramagnetic resonance (EPR)]. We plan to obtain similar correlations for the reduced [2Fe−2S*](SH)$_4$ clusters in two steps. First, we will compute the electronic structures and subsequent **g** tensors as a function of *varying* $Fe^{3+}-Fe^{2+}-S-H$ dihedral angles Ω_1 and Ω_2 on the ferrous side. On the ferric site, the two $Fe^{2+}-Fe^{3+}-S-H$ dihedral angles Ω_3 and Ω_4 have been kept constant because the electronic structure (and subsequent high-spin ferric **g** tensor) is moderately dependent on the ligand orientation. Second, we will apply the theoretical insights to the experimental data (structural and spectroscopic) and compare our analysis with the well-known Bertrand and Gayda model discussed below.

Bertrand and Gayda's Model. In 1979, Bertrand and Gayda (B−G) proposed a simple phenomenological model aimed at rationalizing the variation observed for spectroscopic quantities (**g** tensors, **A** tensors, quadrupole tensors **Q**, and splittings $\Delta E_{\mathbf{Q}}$) among the [2Fe−2S*] proteins and synthetic clusters.[7,8] The authors assumed a local ferrous C_{2v} symmetry, with the sixth d iron orbital Φ_0 being mainly d_{z^2} with a slight admixture of $d_{x^2-y^2}$:

$$\begin{cases} \Phi_0 = \cos\theta(d_{z^2}) + \sin\theta(d_{x^2-y^2}) \\ \Phi_{1,2,3} = d_{xy,xz,yz} \\ \Phi_4 = -\sin\theta(d_{z^2}) + \cos\theta(d_{x^2-y^2}) \end{cases} \quad (1)$$

The angle θ is purely phenomenological ("*this model tells us nothing about the structural significance of the mixing parameter* θ"),[7,8] although it should be linked to some structural features around the ferrous ion, because the nature and relative ordering of the ferrous d orbitals clearly depend on the orientations of the S−ligand bonds. The ferrous **g**-tensor components are then written as (to the first order in θ):

$$\begin{cases} g(Fe^{2+})_{xx} \approx g^0_{xx} + \left\{\dfrac{\sqrt{3}\zeta_{Fe}}{E_3 - E_0}\right\}\theta \approx g^0_{xx} - \left\{\dfrac{4\sqrt{3}\lambda_{Fe}}{E_3 - E_0}\right\}\theta \\ g(Fe^{2+})_{yy} \approx g^0_{yy} - \left\{\dfrac{\sqrt{3}\zeta_{Fe}}{E_2 - E_0}\right\}\theta \approx g^0_{yy} + \left\{\dfrac{4\sqrt{3}\lambda_{Fe}}{E_2 - E_0}\right\}\theta \\ g(Fe^{2+})_{zz} = g^0_{zz} + \left\{\dfrac{2\zeta_{Fe}}{E_1 - E_0}\right\}\theta^2 \approx g^0_{zz} - \left\{\dfrac{8\lambda_{Fe}}{E_1 - E_0}\right\}\theta^2 \end{cases} \quad (2)$$

In eq 2, ζ_{Fe} is the (positive) single-electron spin−orbit coupling constant whereas $\lambda_{Fe} = -\zeta_{Fe}/4$ (for the d^6 ferrous ion). g^0_{xx} and g^0_{yy} are roughly constants ($g^0_{zz} = g_e$). $E_i - E_0$ is

(7) Bertrand, P.; Gayda, J.-P. *Biochim. Biophys. Acta* **1979**, *579*, 107−121.
(8) Guigliarelli, B.; Bertrand, P. In *Advances in Inorganic Chemistry*; Sykes, A. G., Cammack, R., Eds.; Academic Press: 1999; Vol. 147, pp 421−497.
(9) Jung, Y.-S.; Gao-Sheridan, H. S.; Christiansen, J.; Dean, D. R.; Burgess, B. K. *J. Biol. Chem.* **1999**, *274*, 32402−32410.
(10) Lange, H.; Kaut, A.; Lill, R. *Proc. Natl. Acad. Sci. U.S.A.* **2000**, *97*, 1050−1055.
(11) Yeh, A. P.; Chatelet, C.; Soltis, S. M.; Kuhn, P.; Meyer, J.; Rees, D. C. *J. Mol. Biol.* **2000**, *300*, 587.
(12) Meyer, J. *FEBS Lett.* **2001**, *509*, 1−5.
(13) Caldeira, J.; Belle, V.; Asso, M.; Guigliarelli, B.; Moura, I.; Moura, J. J. G.; Bertrand, P. *Biochemistry* **2000**, *39*, 2700−2707.
(14) Coffman, R. E.; Stavens, B. W. *Biochem. Biophys. Res. Commun.* **1970**, *41*, 163−169.
(15) Norman, J. G.; Jackels, S. C. *J. Am. Chem. Soc.* **1975**, *97*, 3833−3835.
(16) Norman, J. G.; Ryan, P. B.; Noodleman, L. *J. Am. Chem. Soc.* **1980**, *102*, 4279−4282.
(17) Noodleman, L.; Baerends, E. J. *J. Am. Chem. Soc.* **1984**, *106*, 2316−2327.
(18) Noodleman, L.; Norman, J. G.; Osborne, J. H.; Aizman, A.; Case, D. A. *J. Am. Chem. Soc.* **1985**, *107*, 3418−3426.
(19) Ueyama, N.; Sugawara, T.; Tatsumi, K.; Nakamura, A. *Inorg. Chem.* **1987**, *26*, 1978.
(20) Bair, R. A.; Goddard, W. A. *J. Am. Chem. Soc.* **1978**, *100*, 5669−5676.
(21) Vrajmasu, V. V.; Bominar, E. L.; Meyer, J.; Münck, E. *Inorg. Chem.* **2002**, *41*, 6358−6371.

the energy difference between the electronic structures $(\Phi_0)^1(\Phi_i)^0$ and $(\Phi_0)^0(\Phi_i)^1$. Because $g_{xy} = 0$, the **g** tensor is diagonalized in the (x, y, z) basis, with $g_{max} = g_{zz}$, $g_{mid} = g_{yy}$, and $g_{min} = g_{xx}$. Moreover, to the first order, g_{xx} and g_{yy} are linear functions of $\sin\theta \sim \theta$ (cf. eq 2), a fact which allows a linear correlation between g_{xx} (and g_{yy}) as a function of $g_{xx} - g_{yy} \approx p + q\theta$ for small variations of θ around zero. The parameters p and q can be determined by a least-squares fitting procedure yielding the $\{E_i\}$'s.

Methodology

DFT Calculations. All of the calculations use the Amsterdam LCAO Density-Functional Programs (ADF 2.3) developed by Baerends and co-workers.[22−27] Unless mentioned otherwise, we used the potential referred to as "VWN−BP" (Vosko, Wilk, and Nusair's exchange and correlation energy[28,29] completed by nonlocal gradient corrections to the exchange by Becke[30] as well as to the correlation by Perdew;[31] corrections included in the self-consistent procedure). We used triple-ζ (plus polarization) basis sets for all of the atoms (Fe, S, C, H).

We computed broken symmetry states for the reduced [2Fe−2S] clusters, states which are not pure $S = {}^1/_2$ spin states but rather states of mixed spin ($M_s = {}^1/_2$) and spatial broken symmetries.[32−34] They are best described within the valence bond approximation and are characterized by the localization of the α-spin 3d electrons on one (high-spin) Fe site and of the β-spin 3d electrons on the other (high-spin) Fe site.

Spectroscopic Values. g Tensors. We computed the total **g** tensor of a $[2Fe-2S^*]^{1+}$ species as a linear combination of the local ferrous $\mathbf{g}(Fe^{2+})$ and ferric $\mathbf{g}(Fe^{3+})$ monomer tensors weighed by proper spin projection coefficients $\{K(Fe)\}$ ($+{}^7/_3$ for the ferric ion, $-{}^4/_3$ for the ferrous one). These $\{K(Fe)\}$ coefficients correspond to the coupling of high-spin ferrous and ferric spins into the total ground-state spin $S = {}^1/_2$ of the cluster:

$$g_{tot} \approx K(Fe^{2+})\,\mathbf{g}(Fe^{2+}) + K(Fe^{3+})\,\mathbf{g}(Fe^{3+}) \qquad (3)$$

The local (i.e., monomer $[FeS_4]$) **g** tensors are computed according to eq 4:

$$\mathbf{g}(Fe)_{ij} \approx g_e\delta_{ij} - \frac{2}{2S_{Fe}}\left(\sum_{maj.} - \sum_{min.}\right)\sum_{k\in[FeS_4]}\sum_{n}\frac{\langle\Phi_0|\zeta_k L_i^k|\Phi_n\rangle\langle\Phi_n|L_j^k|\Phi_0\rangle}{E_n - E_0} \qquad (4)$$

The index k runs over the Fe and S of the given monomer $[FeS_4]$, whereas "maj." and "min." refer to the majority and minority electrons within the monomer, respectively (see Figure 1). Both orbitals are separated by the energy difference $E_n - E_0$. Within the five minority spin−orbital manifold, this energy difference has been systematically determined by computing the Slater state transition ascribing half an electron to both $|\Phi_0\rangle$ and $|\Phi_n\rangle$: $(\Phi_0)^{1/2}(\Phi_n)^{1/2}$. The difference in the corresponding half-occupied molecular orbital energies is then taken as a good estimate of the total energy difference $E_n - E_0$ between the two electronic structures $(\Phi_0)^1(\Phi_n)^0$ and $(\Phi_0)^0(\Phi_n)^1$. The single-electron spin−orbit coupling constants are $\zeta_{Fe} = 410\ cm^{-1}$ and $\zeta_S = 382\ cm^{-1}$.

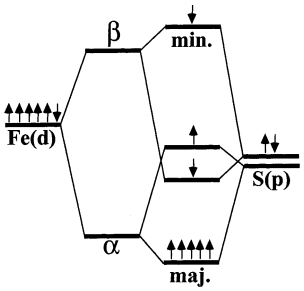

Figure 1. Schematic ferrous site energy level diagram representing the interaction of the Fe(d) and the S,S*(p) atomic orbitals. The large $\alpha-\beta$ split within the Fe(d) orbitals (∼4 eV) is due to the internal exchange polarization. The "maj." and "min." labels refer to the first five d (majority spin α) and the sixth d (minority spin β) orbitals of the high-spin d^6 ferrous ion.

The latter model is very close to the original Noodleman and Baerends' strategy[17] in that both consider only the four (minority spin) d−d transitions on the ferrous side. We included the sulfur contributions, usually on the order of 0.01 while occasionally reaching 0.03, a sulfur correction spread among the three **g**-tensor principal values upon diagonalization. Matrix elements involving the two iron ions or two different sulfur atoms were neglected.[35,36] There are thus formally four types of terms:[36] $\zeta_{Fe}\langle Fe\rangle\langle Fe\rangle$, $\zeta_{Fe}\langle Fe\rangle\langle S_k\rangle$, $\zeta_S\langle S_k\rangle\langle Fe\rangle$, and $\zeta_S\langle S_k\rangle\langle S_k\rangle$ within a given monomer.

Finally, instead of taking arbitrary $\mathbf{g}(Fe^{3+})$-tensor values (2.010, 2.005, 2.006 for Noodleman and Baerends or 2.015, 2.034, 2.030 for B−G), we first decided to set it to a constant $g(Fe^{3+}) = g_{iso} = 2.02$, for the sake of presenting the variations of the three computed g values. This g_{iso} value is supposed to stand for all of the minority spin d−d transition contributions arising from the deep S filled to Fe empty orbitals (see Figure 1). A similar contribution is also found for the ferrous ion; we thus took the same isotropic contribution of 2.02 for it. The next natural step consists of adjusting the three ferric $g(Fe^{3+})_i$ components in order to fit the experimental data. It will be shown below that small deviations from isotropy have significant effects in terms of the total **g** tensors (a source of error originating from the ferric **g** tensor which we cannot master computationnally at this stage) while not affecting the conclusions of this study. For a given $\mathbf{g}(Fe^{3+})$ tensor, we estimate the error for any of the g principal values to be of the order of 0.01.

Magnetic Hyperfine Tensors. The total magnetic hyperfine tensor is $\mathbf{A}_{tot} = \mathbf{A}_{dip} + \mathbf{A}_{orb} + \mathbf{A}_{con}$. We first computed the anisotropic dipolar magnetic hyperfine tensor $\mathbf{A}_{dip}$ for the ferrous ion by adding all of the individual contributions coming from the occupied α and β molecular orbitals. We relied on the following analytical expression:

$$\mathbf{A}_{dip} \approx \left(\frac{g_e\beta_e g_n\beta_n\langle r^{-3}\rangle}{2S}\right)\left(\sum_{\alpha} - \sum_{\beta}\right)\frac{1}{7}[\Xi]_{\alpha,\beta} \qquad (5)$$

where, for a given molecular orbital $\Phi_{\alpha,\beta}$, $[\Xi_{ij}]_{\alpha,\beta} = \langle\Phi_{\alpha,\beta}|T_{ij}|\Phi_{\alpha,\beta}\rangle$

(22) Baerends, E. J.; Ellis, D. E.; Ros, P. *Chem. Phys.* **1973**, *2*, 41−51.
(23) Baerends, E. J.; Ros, P. *Chem. Phys.* **1973**, *2*, 52−59.
(24) Baerends, E. J.; Ros, P. *Int. J. Quantum Chem., Quantum Chem. Symp.* **1978**, *12*, 169−190.
(25) Bickelhaupt, F. M.; Baerends, E. J.; Ravenek, W. *Inorg. Chem.* **1990**, *29*, 350−354.
(26) TeVelde, G.; Baerends, E. J. *J. Comput. Phys.* **1992**, *99*, 84−98.
(27) Ziegler, T. *Chem. Rev.* **1991**, *91*, 651−667.
(28) Vosko, S. H.; Wilk, L.; Nusair, M. *Can. J. Phys.* **1980**, *58*, 1200.
(29) Painter, G. S. *Phys. Rev.* **1981**, *B24*, 4264−4270.
(30) Becke, A. D. *Phys. Rev.* **1988**, *A38*, 3098−3100.
(31) Perdew, J. P. *Phys. Rev.* **1986**, *B33*, 8822−8824.
(32) Noodleman, L.; Norman, J. G. *J. Chem. Phys.* **1979**, *70*, 4903−4906.
(33) Noodleman, L. *J. Chem. Phys.* **1981**, *74*, 5737−5743.
(34) Noodleman, L.; Davidson, E. R. *Chem. Phys.* **1986**, *109*, 131−143.
(35) Stone, A. J. *Proc. R. Soc. London, Ser. A* **1963**, *271*, 24−435.
(36) Atherton, N. M. *Electron Spin Resonance: Theory and Applications*; Halsted Press: New York, 1973.

with $T_{ij} = (3r_ir_j - \delta_{ij}r^2)/r^2$ (the full expression of [Ξ], here computed from *real* d atomic orbitals and dipolar tensor matrix elements, is given in the Supporting Information). The main contribution arises from the sixth (minority spin) d electron of the ferrous ion, with the half-filled shell having a negligible contribution.

The orbital contribution $\mathbf{A}_{orb}$ is taken to first approximation as $P(g(Fe^{2+}) - g_e\mathbf{Id})$, with $P = g_e\beta_e g_n\beta_n\langle r^{-3}\rangle = 87.6$ MHz.[37] Covalency effects are included in the computed local **g** tensor. The uncertainties on $\mathbf{A}_{orb}$ would originate from those in the **g** tensors, that is, of the order of $0.01P$, roughly 1 MHz.

The ionic (core-polarization) isotropic contact term $\mathbf{A}_{con}$ has been calculated[38,39] to be −37.8 MHz (see also ref 37). With a ferrous covalency factor of 0.75,[37] this yields a constant of −28 MHz. B−G had estimated (through a fitting procedure) this last value to be −20 MHz (while assuming an ionic value of −30 MHz and ascribing the difference to covalency effects). An intermediate value of −25 MHz has been obtained in the case of reduced rubredoxin.[21] We will use here B−G's value of −20 MHz, knowing that this only represents a shift (easily dealt with) in the plot of the computed magnetic hyperfine tensor principal values as a function of the Fe−Fe−S−H dihedral angles (as will be seen below, we do not have enough data to perform a fit allowing us to extract a meaningful $\mathbf{A}_{con}$ value for the ferrous site).

Quadrupole Tensors. We computed the quadrupolar tensor **Q** in a similar fashion, as[40]

$$\mathbf{Q} \approx \frac{1}{2}[e^2Q\langle r^{-3}\rangle(1 - R_0)](\sum_{\alpha} + \sum_{\beta})\frac{1}{7}[Z]_{\alpha,\beta} \qquad (6)$$

where $[Z_{ij}]_{\alpha,\beta} = \langle\Phi_{\alpha,\beta}|L_iL_j + L_jL_i - (2/3)\delta_{ij}L(L+1)|\Phi_{\alpha,\beta}\rangle$, Q is the quadrupole moment, and R_0 is the Sternheimer shielding factor. Numerically, $Q = 0.925[Z]$ mm·s^{-1} (the full expression of [Z], here computed from angular momentum components, is given in the Supporting Information).

Notice that, in this section, the *ionic* values for the spin−orbit constants ζ_{Fe} and ζ_S as well as for P are used rather than the *effective* ones (i.e., reduced through covalency effects) because the molecular orbitals inserted in eqs 4−6 are not normalized. An alternative (and equally valid) approach would have consisted of normalizing the molecular orbitals (as in the B−G model) while putting all of the covalency effects into the constants.[21]

Moreover, it can be easily derived from a comparison of both eqs 5 and 6 that the spin-dipolar contribution to the magnetic hyperfine tensor, on the one hand, and the quadrupolar tensor, on the other hand, are proportional (in fact, $[Z_{ij}] = -[\Xi_{ij}]$ through the conversion of the space coordinates into angular momentum operators[41]). Computationally, this proportionality is almost (but not exactly) verified as the sum of the majority spin (α) contributions over all of the occupied (unnormalized) molecular orbitals that do not exactly add up to zero, because this should in principle add up to zero for a half-filled d^5 shell (cf. also refs 5 and 21).

Geometries. Most of our calculations have been performed on a [2Fe−2S*](SH)$_4$ model compound. We verified computationally that the characteristics of the d orbitals as well as the d−d gap values were not drastically changed upon considering SH, SCH_3, SCH_2CH_3, and SCys ligands. The distances and angles were taken from ref 17. In particular, we used on the ferrous site Fe−S* = 2.28 Å and Fe−S(H) = 2.38 Å and on the ferric site Fe−S* = 2.21 Å and Fe−S(H) = 2.31 Å. The Fe−Fe direction is taken as the *z* axis. The inorganic-bridging sulfur atoms S* lie in the *xz* plane, and the terminal-ligating sulfur atoms S lie in the *yz* plane.

We rotated the S−H bond around the Fe−S bond by steps of 15° on the ferrous site. The two Fe^{3+}−Fe^{2+}−S−H dihedral angles $\Omega_{1,2}$ thus vary from −180° to +180°. For symmetry reasons, we can actually restrain Ω_1 to 0−180°. The two Fe^{2+}−Fe^{3+}−S−H dihedral angles $\Omega_{3,4}$ on the ferric site were kept constant (i.e., 0°). We have computed the **g** tensors for the two cases for which at least two symmetry elements are kept. This greatly simplifies the computation of the Slater d−d transitions, because the five d orbitals then fall into two sets. In the first case, the local symmetry on the ferrous site is C_2: $\Omega_1 = \Omega_2$ ($0° \le \Omega_i \le 180°$). The d orbitals are separated into $\{d_{z^2}, d_{x^2-y^2}, d_{xy}\}$ and $\{d_{xz}, d_{yz}\}$. The configuration $\Omega_1 = \Omega_2 = 0°$ corresponds to the starting point of the B−G model, whereas Noodleman and Baerends considered the two configurations $\Omega_1 = \Omega_2 = 0°$ or 180° in their calculations.[17] In the second case, the local (and global) symmetry is lowered to C_s, that is, $\Omega_2 = -\Omega_1$. The d orbitals are now separated into $\{d_{z^2}, d_{x^2-y^2}, d_{xz}\}$ and $\{d_{xy}, d_{yz}\}$.

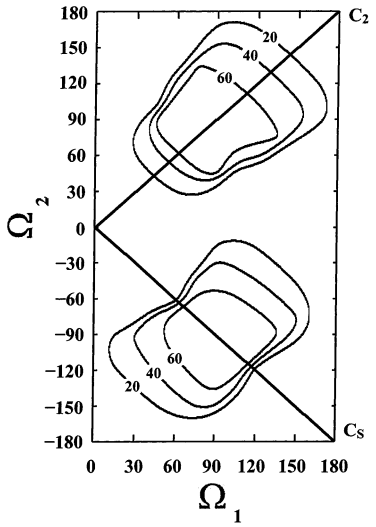

Figure 2. Contour plot of the d_{xy} contribution (%) to the sixth d ferrous orbital Φ_0 as a function of the two Fe−Fe−S−H dihedral angles for the [2Fe−2S*](SH)$_4$ model. The two lines labeled "C_2" and "C_s" represent the two paths defined by special relationships between Ω_1 and Ω_2 (see main text).

Convergence Problems. Great care had to be taken for the calculations of the electronic structures. In effect, there were cases where different electronic structures (i.e., differing by the orbital occupied by the sixth d ferrous electron) corresponded to the same occupation scheme. This occurs when two electronic structures are almost degenerate. The correct ordering of the two close d orbitals is then derived from a Slater transition-state calculation ascribing half an electron to each orbital.

Results

d_{z^2}/d_{xy} Mixing. In Figure 2 the d_{xy} Mulliken spin population in the molecular orbital Φ_0 is plotted as a function of (Ω_1, Ω_2). There are two regions in the phase space where d_{xy} becomes dominant (spin population greater than 60%) centered around (90°, 90°) and (90°, −90°). This graph is complementary to that drawn for d_{z^2} (Figure S1 in the

(37) Mouesca, J.-M.; Noodleman, L.; Case, D. A.; Lamotte, B. *Inorg. Chem.* **1995**, *34*, 4347−4359.
(38) Freeman, A. J.; Watson, R. E. In *Magnetism*; Rado, G. T., Suhl, H., Eds.; Academic Press: New York, 1965; Vol. IIA, p 167.
(39) Watson, R. E.; Freeman, A. J. *Hyperfine Interactions*; Academic Press: 1967.
(40) Zimmermann, R.; Ritter, G.; Spiering, H.; Nagy, D. L. *J. Phys. C: Solid State Phys.* **1974**, *6*, 439−442.
(41) Stevens, K. W. H. *Proc. Phys. Soc., London, Sect. A* **1952**, *65*, 209.

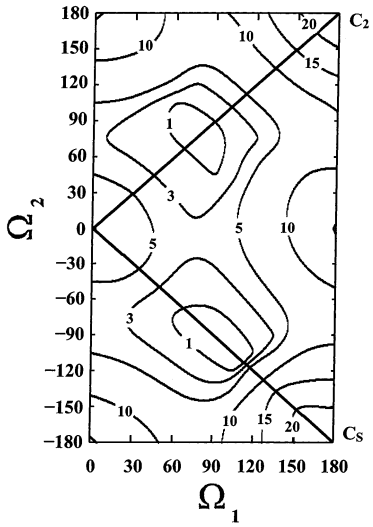

Figure 3. Contour plot of the $d_{x^2-y^2}$ contribution (%) to the sixth d ferrous orbital Φ_0 as a function of the two Fe−Fe−S−H dihedral angles for the $[2Fe-2S^*](SH)_4$ model. The two lines labeled "C_2" and "C_s" represent the two paths defined by special relationships between Ω_1 and Ω_2 (see main text).

Supporting Information). In other words, the highest-occupied molecular orbital (HOMO) is essentially of the d_{z^2} character in the regions where d_{xy} fades: (0°, 0°), (0°, ±180°), (+180°, 0°), and (+180°, ±180°). In Figure 3 the same type of graph is shown for $d_{x^2-y^2}$. Its weight is not greater than 10% except for small regions (+180°, ±180°). $d_{x^2-y^2}$ almost vanishes in the two regions where d_{xy} dominates.

The full computation of the **g**-tensor components (principal values and vectors) is easier for the C_2 and C_s cluster symmetries. These symmetries are realized in Figures 2 and 3 along two paths, starting from the B−G region (0°, 0°) and going straight to (+180°, +180°) (C_2) or (+180°, −180°) (C_s). With no symmetry, the five ferrous d orbitals are mixed and split, and the computation of the d−d transitions becomes rather tedious because most of the Slater states do not converge properly.

The HOMO−LUMO gap (LUMO for the lowest-unoccupied molecular orbital) obtained from a Slater transition procedure in the same phase space is plotted in Figure S2 in the Supporting Information. The maximal gaps (larger than 300 meV) are found where d_{z^2} dominates. Where d_{xy} dominates, the gap is found to be between 100 and 200 meV. The HOMO−LUMO gap is exactly zero at two points along the C_s path, around (+60°, −60°) and (+120°, −120°).

***C*$_2$ Calculations.** The overall geometry of the cluster is constrained to C_2 ($\Omega_1 = \Omega_2$). It can be seen from Figures 2 and 4 that the transition from d_{z^2} to d_{xy} is done smoothly; both of the orbitals belong to the same representation and therefore mix along the C_2 path. Correspondingly, the d−d gap is always different from zero (Figure S2 in the Supporting Information). In Figure 5 the variations of the three *g* principal values as a function of the two $Fe^{3+}-Fe^{2+}-S-H$ equal dihedral angles are represented. Many features are noticeable: first, the range of the *g* values (1.80−2.05) is quite comparable to what is experimentally observed for the B−G "1.96" class. In particular, g_{max} is the largest around

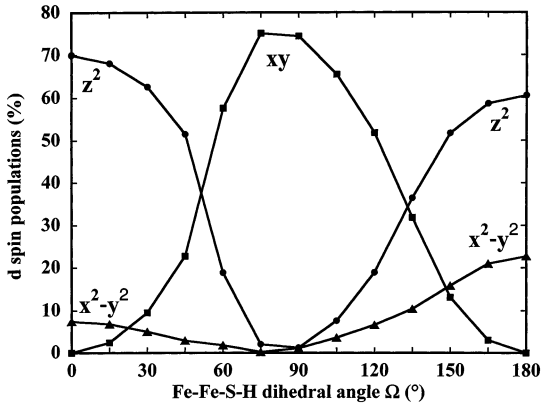

Figure 4. Contribution (%) of the d_{xy} (squares), d_{z^2} (circles), and $d_{x^2-y^2}$ (triangles) to the sixth d ferrous orbital Φ_0 along the C_2 path as a function of Ω (=$\Omega_1 = \Omega_2$).

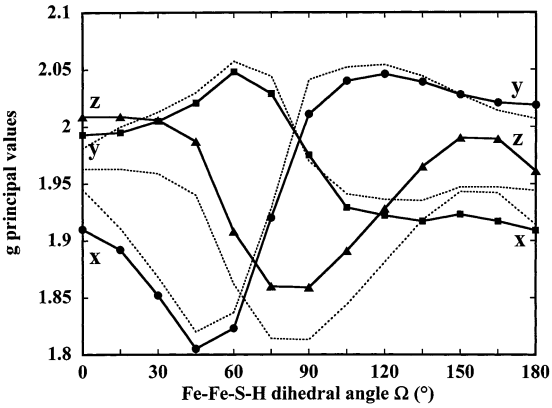

Figure 5. Computed **g**-tensor principal values for the $[2Fe-2S^*](SH)_4$ model as a function of Ω (=Ω_1) along the C_2 path ($\Omega_1 = \Omega_2$). The solid lines are drawn for an isotropic $\mathbf{g}(Fe^{3+})$ tensor (2.02). The dotted lines are drawn for an anisotropic $\mathbf{g}(Fe^{3+})$ tensor (2.025 along *x*, 2.020 along *y*, and 2.000 along *z*).

$\Omega_1 = \Omega_2 \approx 60°$ and 120°. Second, and most important for our discussion, the **g** tensor is axial around the same 60° and 120° angle values. *There is no such axiality around 0° or 180°*. A third point deals with the principal vectors. One of the principal vectors, let us say $\mathbf{V}_1$, stays aligned with the *z* axis, for symmetry reasons. A second one, $\mathbf{V}_2$, goes from *x* to *y* for the dihedral angle Ω varying from 0° to 180° (the remaining vector $\mathbf{V}_3$ goes from *y* to *x*). More precisely, between 120° and 150°, $\mathbf{V}_1$ is associated with g_{mid}, $\mathbf{V}_2$ (close to *y*) is associated with g_{max}, and $\mathbf{V}_3$ (close to *x*) is associated with g_{min}.

***C*$_s$ Calculations.** For the second C_s path ($\Omega_2 = -\Omega_1$), the transition from d_{z^2} to d_{xy} is abrupt because these atomic orbitals do not mix. There are two points along this C_s paths for which the d−d gap becomes exactly zero. It can be foreseen that one of the $\{g_i\}$ values will then diverge for our model as the second-order perturbation breaks down. Moreover, the *g* values are never greater than 2.02. Two *g* components are close for a large Ω_1 (=$-\Omega_2$) range (0−120°). The **g** tensor becomes axial only around 160°.

In Figure 6 one principal vector is kept aligned with the *y* axis for symmetry reasons. The two other principal vectors go from *x* (respectively *z*) to *z* (respectively *x*) for Ω varying from 0° to 180°.

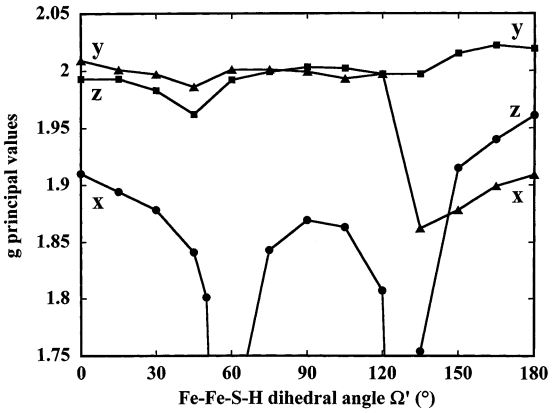

Figure 6. Computed **g**-tensor principal values for the [2Fe−2S*](SH)$_4$ model as a function of Ω (=Ω$_1$) along the C_s path (Ω$_2$ = −Ω$_1$). The solid lines are drawn for an isotropic **g**(Fe^{3+}) tensor (2.02).

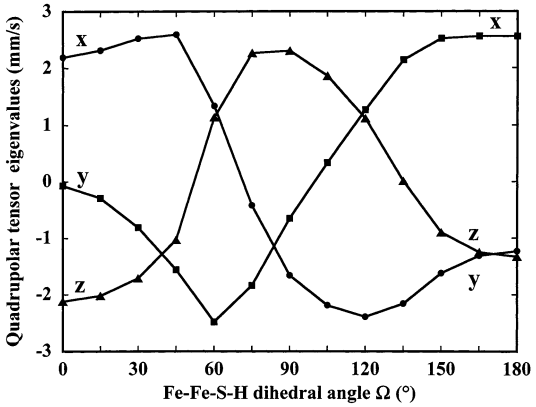

Figure 7. Computed quadrupolar tensor **Q** principal values for the [2Fe−2S*](SH)$_4$ model as a function of Ω (=Ω$_1$) along the C_2 path (Ω$_1$ = Ω$_2$).

Quadrupole Tensors Q. We computed the quadrupole tensor in the C_2 symmetry case. The three components are plotted in Figure 7. One principal vector is kept aligned with the *z* axis for symmetry reasons. The two other principal vectors go from *x* (respectively *y*) to *y* (respectively *x*) for Ω varying from 0° to 180°.

Magnetic Hyperfine Tensors. The *three* components (contact + dipolar + orbital) of the total ferrous ion magnetic hyperfine tensor as a function of Ω$_1$ = Ω$_2$ (in C_2 symmetry) were plotted (Figure 8). The principal vectors of the **A**$_{tot}$ tensor follow closely with those of the quadrupole tensor (the main contribution to **A**$_{tot}$ being the dipolar term, proportional to **Q**).

Discussion: Application to the Proteins

Generalities. Let us first set the conceptual framework of our discussion. At first approximation, there are only two relevant physical variables in our [2Fe−2S*](SH)$_4$ models: the two dihedral angles Ω$_1$ and Ω$_2$. We verified that the effect of small changes in the geometry is negligible compared to that of the orientation of the ligand−sulfur lone pairs. This is true for changes in the Fe_2S_2 core geometry, any of the interatomic distances, and the ferric site local geometry. For example, we compared the electronic structure of the *Anabaena* [2Fe−2S*] cluster (including the four cysteines) to that of its corresponding "ideal" C_2 model, only to find

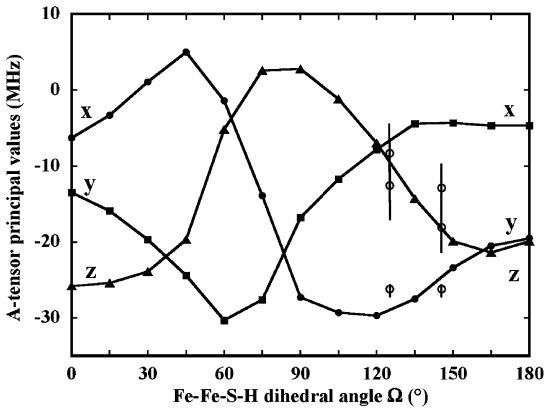

Figure 8. Computed magnetic hyperfine tensor **A**$_{tot}$ principal values for the [2Fe−2S*](SH)$_4$ model as a function of Ω (=Ω$_1$) along the C_2 path (Ω$_1$ = Ω$_2$).

them almost identical in terms of the electronic structures and resulting spectroscopic values.

From a general point of view, each component of the **g** tensor (or of any tensor) depends linearly, to the first order, on δΩ$_1$ and δΩ$_2$ (variations of the dihedral angles around a fixed set of values Ω$_1^0$ and Ω$_2^0$ defining a given geometry):

$$g_i \approx g_i(\Omega_1^0,\Omega_2^0) + \left(\frac{\partial g_i}{\partial \Omega_1}\right)_{\Omega_1^0} \delta\Omega_1 + \left(\frac{\partial g_i}{\partial \Omega_2}\right)_{\Omega_2^0} \delta\Omega_2 \qquad (7)$$

To draw linear plots (such as those proposed by B−G), we need to move along a *path* in the (Ω$_1$, Ω$_2$) phase space, defined by an *explicit* relationship between Ω$_1$ and Ω$_2$ under the form Ω$_1$ = f_1(Ω) and Ω$_2$ = f_2(Ω). Then Ω becomes the only variable of the problem (for example, along the C_2 path: f_1(Ω) = f_2(Ω) = Ω). One can generally compute to the first order in δΩ the {g_i} values around a given Ω value along the chosen path:

$$g_i \approx g_i(\Omega^0) + \left[\left(\frac{\partial g_i}{\partial f_1}\right)\left(\frac{\partial f_1}{\partial \Omega}\right) + \left(\frac{\partial g_i}{\partial f_2}\right)\left(\frac{\partial f_2}{\partial \Omega}\right)\right]\delta\Omega \qquad (8)$$

From this, it is always possible to plot g_{mid} and g_{min} as a function of Ω. The slopes of these plots depend on the mean point Ω^0 in the (Ω$_1$, Ω$_2$) phase space describing the systems as well as on the path followed. In other words, one can draw a different set of linear plots for each "geometrically homogeneous" class of [2Fe−2S*] defined by their average Ω^0 value, whether they are proteins or synthetic analogues.

Correlation between the {g_i} Values and the Local Ferrous Ion Environment. To define geometrically homogeneous classes of [2Fe−2S*] systems, the *four* Fe−Fe−S−C$_\beta$ dihedral angles {Ω$_i$}$_{i=1-4}$ for a wide selection of *oxidized* proteins whose crystallographic structures have been found in the Protein Data Bank[42] (PDB) were plotted in Figure 9. To our knowledge, only one structure in the *reduced* state has been published so far, that of *Anabaena*, obtained at an atomic resolution in both the oxidized (1.30 Å) and reduced (1.17 Å) states (PDB ID: 1CZP).[43] To check

(42) Berman, H. M.; Westbrook, J.; Feng, Z.; Gilliland, G.; Bhat, T. N.; Weissig, H.; Shindyalov, I. N.; Bourne, P. E. *Nucleic Acids Res.* (http://www.pdb.org/) **2000**, *28*, 235−242.

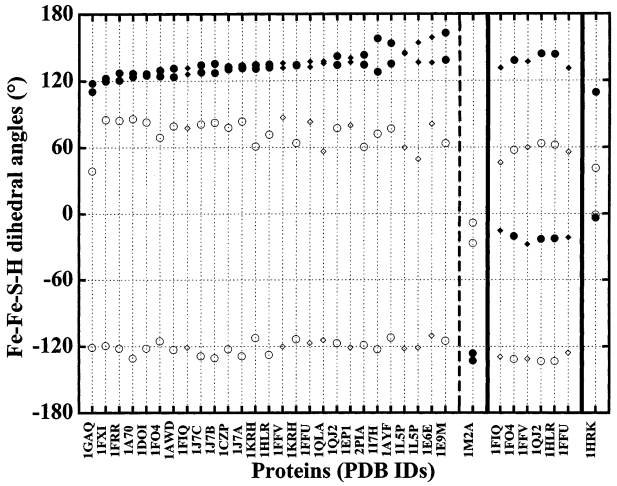

Figure 9. Dihedral angles Fe−Fe−S−C_β for [2Fe−2S*] proteins with corresponding crystallographic structures stored in the PDB. Proteins are classified in three classes (A, B, and C) with respect to the similarity of their dihedral angles. Class A groups plant-type ferredoxins, class B groups the xanthine oxidases, and class C has only one member. For class A, the solid circles stand for the two ligands (structurally analogous to the reduced *Anabaena* ferrous site) on one iron side of the clusters in relatively precise oxidized structures (see main text), while the open circles stand for the other (putatively ferric) iron site (in reduced *Anabaena* protein, the effectively oxidized site). Solid and open diamonds stand for less precise data. For classes B and C, we followed the same code (circle/diamond and solid/open based on structural analogies with class A) without presuming the redox nature of the iron sites.

the stereochemical quality of the protein structures, we ran PROCHECK[44,45] on all of the PDB files and retained only the "best" structures in our view. These were defined by combining criteria such as the resolution, percentage of residues in the most-favored regions of a Ramachandran plot, and other main-chain and side-chain parameter statistics offered by PROCHECK.

Three classes are clearly distinguishable in Figure 9. The first and the most important in terms of the number of representatives, class A, mainly matches the plant, mammalian, and bacterial ferredoxins. Still, other representatives of the same class A are the ferredoxin-like clusters, as found in the xanthine oxidase family. The identification of the putative ferrous iron sites is based on their structural analogies with the known ferrous site of the *Anabaena* system,[43] in terms of the dihedral angles, the larger number of hydrogen bonds relative to the other iron site, and the closeness of the putative ferrous ion to the protein surface. The two (Fe^{3+}−Fe^{2+}−S−C_β) dihedral angles ($\Omega_1 < \Omega_2$) are close to one another ($\Omega_{av} = (\Omega_1 + \Omega_2)/2 \approx 135°$ with $\Delta\Omega \approx \pm 15°$ for the whole class). It can be noticed in passing that, for large dihedral angles ($\geq 140°$), Ω_1 and Ω_2 tend to differ significantly as compared to all of the systems characterized by lower Ω_{av} values ($\leq 140°$).

The proteins of class A have been classified according to their increasing average dihedral angle Ω_{av}. It is then clear

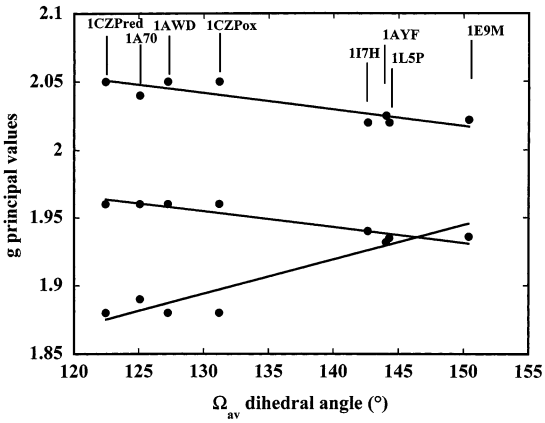

Figure 10. Experimental **g** principal values plotted as a function of Ω_{av}. Solid circles: class A systems (plant, mammalian, and bacterial fdxs). The *Anabaena* **g**-tensor values are plotted for both of the redox structures ($\Omega_{av} \approx 131°$ in the oxidized structure and $\Omega_{av} \approx 122°$ in the reduced structure). The $\{g_i\}$ values are taken from the following references: 1CZP,[46] 1A70,[53] 1AWD,[66] 1FIQ,[13] 1FFV,[81] 1HLR,[13] 1I7H,[82] 1AYF,[53] 1L5P,[83] and 1E9M.[84]

from Figure 9 that both Ω_1 and Ω_2 are correlated; that is, the local geometry is to the first approximation C_2. We should therefore observe a correlation between the three $\{g_i\}$ principal values and Ω_{av}. Before testing that hypothesis, let us mention quickly that the second class (class B), the nonclassic "xanthine oxidase" (XO) type family, is characterized by an iron site, which is geometrically close to the assumed ferric site of class A. The other iron site differs from that of class A (dihedral angles around +130° and −20°). We found only one representative in the third class (class C), a human ferrochelatase (PDB ID: 1HRK). One iron site is common between classes B and C.

Figure 10 shows the three $\{g_i\}$ principal values as a function of Ω_{av}. At first sight, Figure 10 resembles the previously demonstrated B−G diagram (i.e., the plots of g_{mid} and g_{min} as a function of θ). However, there is a fundamental difference: the axis variable is no longer phenomenological (θ) but structural (Ω_{av}). Moreover, the plots of Figure 10 are independent from any model. It is the first time to our knowledge that such an electronic/structural correlation has been established for the [2Fe−2S*] clusters. Upon closer examination, the linear plots are rather well defined ($R \geq 0.9$ in each case). This is particularly the case for the largest component g_{max}, which is parallel to g_{mid} (in constrast with g_{max} plotted as a function of $g_{mid} - g_{min}$). The g_{mid} and g_{min} plots slope in opposite directions; the slope of g_{mid} is roughly 2 times smaller in magnitude than that of g_{min}.

There are still some restrictions to the structural conclusions that can be drawn from Figure 10. First, almost all of these proteins have been crystallized in their oxidized state, with one exception (*Anabaena*).[43] One can suppose that the local conformation is not drastically changed upon reduction. We plotted the *Anabaena* data for both the oxidized structure, for the sake of consistency with the other angles we used, and the reduced structure. Second, and consequently, we do not always know which iron site is being reduced in vivo or in vitro. Experimental data, other than crystallographic data, could be availed of to partially answer this dilemma

(43) Morales, R.; Charon, M.-H.; Hudry-Clergeon, G.; Pétillot, Y.; Norager, S.; Medina, M.; Frey, M. *Biochemistry* **1999**, *38*, 15764−15773.
(44) Morris, A. L.; MacArthur, M. W.; Hutchinson, E. G.; Thornton, J. M. *Proteins* **1992**, *12*, 345−364.
(45) Laskowski, R. A.; MacArthur, M. W.; Moss, D. S.; Thornton, J. M. *J. Appl. Crystallogr.* **1993**, *26*, 283−291.

(differential number of H bonds, temperature-dependent NMR experiments, etc.).

Computed g Tensors. It can be seen from Figure 10 that the experimental **g** tensor is axial around $\Omega_{av} \approx 145°$ and acquires its rhombicity for lower dihedral angles (down to 120°). However, our model (continuous lines in Figure 5) predicts the axiality around 120°. This discrepancy is easily resolved. We considered an *isotropic* ferric site **g**-tensor value of 2.02 in our model; it can now be shown how sensitive the total **g**-tensor values are to the introduction of a slight anisotropy on the ferric site. This, in turn, can very easily move the crossing point between g_{mid} and g_{min}. We searched for a ferric **g** tensor shifting the crossing point from 120° to more than 140°, and we found the three ferric principal values 2.025, 2.020, and 2.000 (along *x*, *y*, and *z*, respectively; see Figure 5). This procedure only shifts the three $\{g_i\}$ values vertically without significantly altering their corresponding principal vectors and overall shapes. Figures 5 and 10 thus compare well in terms of $\{g_i\}$ values and slopes.

For the sake of comparison, we computed the **g** tensor for a [2Fe−2S*](SH)$_4$ model directly constructed from the reduced *Anabaena* ferredoxin (PDB ID: 1CZP) and obtained the following principal values: 2.049 (along the bisector between the $+x$ and $-y$ axes), 1.967 (along the bisector between the *x* and *y* axes), and 1.954 (along the *z* axis), again assuming an isotropic ferric **g** tensor of 2.02. The experimental values are rhombic: 2.05, 1.96, and 1.88.[46] Again, these principal values are very sensitive to slight anisotropies of the ferric site tensor: for 1CZP we compute 2.053 (along the bisector between the $+x$ and $-y$ axes), 1.978 (along the bisector between the *x* and *y* axes), and 1.908 (along the *z* axis) with the ferric components 2.025 (along the *x* axis), 2.020 (along the *y* axis), and 2.000 (along the *z* axis), determined above for idealized C_2 geometries.

Class A corresponds to a region where the weights of both the d_{z^2} and d_{xy} orbitals in Φ_0 are important (the d_{xy} and d_{z^2} spin populations, 50% and 20%, respectively, for $\Omega_{av} = 120°$ are reversed at $\Omega_{av} = 150°$). Our computed $\{g_i\}$ values compare well with the experimental values when plotted as a function of Ω_{av} (Figure 5). Moreover, the g_{max} values reach a maximum (2.04) in that region of the phase space. Our calculations show that the main magnetic axis (corresponding to g_{max}) is roughly aligned along *y* (the deviation from *y* being due to a small admixture of *x*) in the (120−150°) Ω_{av} range. Finally, the theoretical range of $10^2(g_{mid} - g_{min})$ matches that observed experimentally (∼8).

Finally, let us comment on the computed d−d transitions (through the Slater procedure) in the (120−150°) dihedral angle Ω_{av} region. First, the orbitals involved are, in fact, mixtures of the d ferrous orbitals, contrary to the C_{2v} results of Noodleman and Baerends yielding unmixed atomic d orbitals. In our case (C_2 symmetry), let us call $d_{xy} + \epsilon d_{z^2}$ the lowest occupied orbital and $d_{z^2} + \epsilon d_{xy}$ the first unoccupied one (a correct description at $\Omega_{av} = 120°$; at $\Omega_{av} = 150°$, the relative proportions of d_{xy} and d_{z^2} would actually be reversed). Moreover, in C_2 symmetry, the d_{xz} and d_{yz} orbitals do mix together into positive (i.e., $d_{xz} + d_{yz}$) and negative (i.e., $d_{xz} - d_{yz}$) linear combinations. We found over the Ω_{av} range the following d−d transition values: 2400−3200 cm^{-1} for $d_{xy} + \epsilon d_{z^2} \rightarrow d_{z^2} + \epsilon d_{xy}$, 4000−5200 cm^{-1} for $d_{xy} + \epsilon d_{z^2} \rightarrow d_{xz} - d_{yz}$, and 4800−7200 cm^{-1} for $d_{xy} + \epsilon d_{z^2} \rightarrow d_{xz} + d_{yz}$, respectively. These values match rather well with the three experimentally observed transitions. The first one is measured as 500−2000 cm^{-1}, 500 cm^{-1} from the spinach temperature dependence of the ferrous site quadrupole splitting;[47] the transition for putidaredoxin is larger than 860 cm^{-1},[48] with that for adrenodoxin being even larger (from the magnetic susceptibility Curie law observed up to room temperatures[49]). The two other transitions are measured at 3800−4500 and 5800−6000 cm^{-1} (from infrared spectroscopy applied on both spinach and adrenodoxin ferredoxins),[50] respectively (all of the value ranges as reported in ref 7 and 17). The lowest d−d transition thus increases from spinach to adrenodoxin, as predicted in our model (cf. Figure S2 in the Supporting Information and the end of the above d_{z^2}/d_{yz} Mixing section).

Computed Q Tensors. The fitting procedure of a Mössbauer spectrum yields the *relative* angle between the **A** and **Q** principal vectors rather than the relative angle between the **g** and **Q** principal vectors. It is still possible in some instances to obtain the relative orientations of the **g** and **A** principal vectors by relying on the ENDOR experiments. When this is feasible, the relative orientation of the **g** and **Q** principal vectors can be indirectly derived.

In the present paper, there is no adjustable parameter in the calculation of the $\Delta E_{\mathbf{Q}}$ values (as there was for the ferric tensor components in the calculation of the **g** tensor). We computed the angle between the g_{max} and Q_{max} principal vectors. They are orthogonal, except for $\Omega_{av} = 60°$ (not structurally relevant) and in the range 105−135° (relevant for the class A proteins: for $\Omega_{av} \approx 120°$, the **g** tensor is rhombic). This matches the experimental results.[47,48,51] In effect, what is measured in Mössbauer is the largest (in absolute value) quadrupole principal value. Therefore, the main magnetic axis (the g_{max} principal vector) is collinear to the principal vector associated with the largest (in absolute value, while negative) **Q** principal value in the case of the spinach-like systems ($\Omega_{av} \approx 120°$), whereas they are orthogonal for the putida-like systems ($\Omega_{av} \approx 150°$, the largest principal value being positive).

Computed Magnetic Hyperfine Tensors. For $\Omega = 150°$ (axial **g** tensor), the magnetic hyperfine tensor is found close to (disklike) axiality (−23, −20, −4 MHz). For $\Omega = 120°$ (rhombic **g** tensor), the magnetic hyperfine tensor is close to (cigarlike) axiality (−30, −8, −7 MHz).

(46) Cheng, H.; Xia, B.; Reed, G. H.; Markley, J. L. *Biochemistry* **1994**, *33*, 3155−3164.

(47) Dunham, W. R.; Bearden, A. J.; Salmeen, I. T.; Palmer, G.; Sands, R. H.; Orme-Johnson, W. H. *Biochim. Biophys. Acta* **1971**, *253*, 134−152.

(48) Anderson, R. E.; Dunham, W. R.; Sands, R. H.; Bearden, A. J.; Crespi, H. L. *Biochim. Biophys. Acta* **1975**, *408*, 306−318.

(49) Kimura, T.; Tasaki, A.; Wateri, H. *J. Biol. Chem.* **1970**, *245*, 4450−4452.

(50) Eaton, W. A.; Palmer, G.; Free, J. A.; Kimura, T.; Lovenberg, W. *Proc. Natl. Acad. Sci. U.S.A.* **1971**, *68*, 3015−3020.

(51) Münck, E.; Debrünner, P. G.; Tsibris, J. C. M.; Gunsalus, I. C. *Biochemistry* **1972**, *11*, 855−863.

As far as a comparison with experimental data, let us stress once more that, in our model, we need to have available, for a given system, both a crystallographic structure (at least in its oxidized state) and spectroscopic data (in the reduced state). In the case of magnetic hyperfine tensors, this is (to the best of our knowledge) only possible for two systems. Comparison is made here (as in the B−G paper) for intrinsic (before spin coupling) magnetic hyperfine tensors.

For the (bovine) adrenodoxin (PDB ID: 1AYF[52]), we have the corresponding (though measured by ENDOR for the *pig* adrenodoxin[53,54]) intrinsic (ferrous) magnetic hyperfine components: -12.8 ± 3, -18.0 ± 3, and -26.3 ± 1 MHz. The very same values have been reported for the (*Pseudomonas putida*) putidaredoxin (pdx),[53,54] whereas other authors[51] proposed slightly alternative values for this last native pdx protein (Mössbauer measurements): -10.5 ($+2$, -1), -15.8 ± 3, and -26.3 ± 1 MHz.

For the (*Spinacia oleracea*) spinach ferredoxin (PDB ID: 1A70[55]), the Mössbauer magnetic hyperfine components are as follows:[47,54] -8.3 ± 4, -12.6 ± 4, and -26.5 ± 1 MHz. The last value (-26.5 MHz) has also been reported by Fritz et al.[53] (ENDOR).

We first notice that both adrenodoxin (adx) and spinach ferredoxin magnetic hyperfine tensors do not have the same isotropic values: -19.0 MHz (-17.5 MHz for pdx[51]) and -15.8 MHz, respectively. At first view, these small (though significant) changes are not due to variations in the isotropic orbital contribution[37] because the class A **g** tensors have the same isotropic value (1.96) but are most probably related to different hyperfine contact values. Moreover, it has been recently observed[5] that the pdx ENDOR values for the first two components, reported by Sands and Dunham,[53,54] are ca. 20% too large, not being compatible with the corresponding Mössbauer data. We do not know however if such a correction would have to be also applied to the adx data. If corrected as suggested for pdx, one would have rather -10.2, -14.4, and -26.3 MHz (unchanged), which is an isotropic value of -17.0 MHz (quite similar to that of pdx) but still larger in magnitude than that of spinach.

We plotted the experimental points for spinach (lower angle values), for which good agreement is found between the predicted and measured values (as was already the case for the B−G model).

In the absence of the new Mössbauer data on adx,[56] we reported in Figure 8 the original ENDOR data by Fritz et al.[53] As can be seen, the agreement between theory and experiment is poor in that case (as also pointed out for pdx between the data and the B−G model[5]). Clearly therefore, in this (upper dihedral angle values) region of axial **g** tensors, more experimental work (especially Mössbauer) has to be performed in order to better test our theory.

In particular, let us mention here the paper by Fox et al.[57] done on the methane monooxygenase (MMO) reductase. Upon studying by Mössbauer the ferrous site of the reduced [2Fe−2S] cluster of MMO, these last authors[57] encountered a difficulty in that the A_{min} and A_{mid} components of the magnetic hyperfine tensor were highly correlated with the **Q**-tensor asymmetry factor η. By fixing the value of η and least-squares fitting the ferrous site Mössbauer spectra, they obtained fits of comparable quality: the values of A_{min} and A_{mid} diverge as η decreases (cf. Figure 18 of ref 57). Note that this artifactual problem related to the fitting procedure itself is disconnected from our own (and B−G's) prediction that A_{min} and A_{mid} will diverge as η increases, constitutive of the fact that the quadrupolar and the magnetic dipolar hyperfine tensors are proportional (cf. the Supporting Information).

Comparison between Our Model and That of B−G. One of the main differences between our model and that of the B−G model lies in the fact that the correlating parameter is structural in our case (Ω_{av}) and phenomenological in B−G's case (θ is an iron d atomic orbital mixing coefficient). Closely related to the first point, B−G assumed the local ferrous geometry to be C_{2v}, whereas experimentally and in our model, it is found to be close to C_2 for the class A proteins. Consequently, the nature of Φ_0 containing the sixth d ferrous electron is different, with our DFT calculations showing the major role played by the d_{xy} contribution in Φ_0.

The B−G model is designed to fit the experimental $\{g_i\}$ values when plotted as a function of $g_{mid} - g_{min}$ by means of adjustable parameters, the energetic gaps $E_i - E_0$. Our task was more challenging as we tried to reproduce these same experimental values without free parameters (apart from the ferric **g**-tensor components). The main difference between B−G's and this paper lies in the prediction of the **g**, $\mathbf{A}_{tot}$, and **Q** tensor principal vectors. Within a common reference frame (z along Fe−Fe and x along S*−S*), we found the g_{max} principal vector to be closest to y when **g** is axial ($\Omega_{av} \approx 150°$), whereas B−G predict it to be along z. For a rhombic **g** tensor ($\Omega_{av} \approx 120°$), the principal vector associated with g_{max} is close to the bisector between the $+x$ and $-y$ axes in our case. The same observation is true for the magnetic hyperfine and quadrupole tensors. In some circumstances (as in the study of the interaction of the two paramagnetic centers, one of them at least being a [2Fe−2S*] cluster), the choice made in the orientation of the **g**-tensor principal values may turn out to be crucial for the interpretation of the resulting EPR spectra.

It is interesting to note an experimental study aimed at determining the spin population distribution and the **g**-tensor orientation of a reduced [2Fe−2S] cluster, found in the ferredoxin from *Arthrospira (Spirulina) platensis* (PDB ID: 4FXC,[58] oxidized structure at 2.5 Å). The three g values

(52) Müller, A.; Müller, J. J.; Müller, Y. A.; Uhlmann, H.; Bernhardt, R.; Heinemann, U. *Structure* **1998**, *6*, 269−280.
(53) Fritz, J.; Anderson, R.; Fee, J.; Palmer, G.; Sands, R. H.; Tsibris, J. C. M.; Gunsalus, J. C.; Orme-Johnson, W. H.; BeEinert, H. *Biochim. Biophys. Acta* **1971**, *253*, 110−133.
(54) Sands, R. H.; Dunham, W. R. *Q. Rev. Biophys.* **1975**, *7*, 443−504.
(55) Binda, C.; Coda, A.; Aliverti, A.; Zanetti, G.; Mattevi, A. *Acta Crystallogr., Sect. D: Biol. Crystallogr.* **1998**, *54*, 1353.
(56) Cammack, R.; Rao, K. K.; Hall, D. O.; Johnson, C. E. *Biochem. J.* **1971**, *125*, 849−856.
(57) Fox, B. G.; Hendrich, M. P.; Surerus, K. K.; Andersson, K. K.; Froland, W. A.; Lipscomb, J. D.; Münck, E. *J. Am. Chem. Soc.* **1993**, *115*, 3688−3701.

(2.052, 1.957, 1.887) as well as the $\{\Omega_i\}$ dihedral angles (131.4°, 140.0°, 70.9°, −130.4°) are typical of a class A (plantlike) ferredoxin. The authors found the plane defined by the principal vectors associated with g_{max} and g_{mid} to be parallel to that containing the two Fe and the four S(Cys) atoms, with the g_{mid} principal vector roughly oriented along the Fe−Fe *z* axis and the g_{max} principal vector roughly oriented along the *y* axis. They consequently found the plane defined by the g_{mid} and g_{min} principal vectors to be close to the 2Fe−2S* plane; that is, the g_{min} principal vector is oriented along the S*−S* *x* axis. As can be readily seen, their experimental results almost perfectly match our theoretical predictions while contradicting those of B−G.

If the **g**-tensor *principal values* are considered alone, it is still possible to link both B−G and our models by setting $\Omega_{av} \approx 117.4 - 1.53\Theta$ or $\Theta \approx 76.3 - 0.65\Omega_{av}$. This would still be rather artificial because, in the present study, the d_{xy} contribution in Φ_0 plays a major role in the computation of the spectroscopic values. More precisely, the relative contributions of d_{xy} to the $\{g_i\}$ values is dominant around $\Omega_{av} \approx 120°$, while that of $d_{x^2-y^2}$ becomes more important as Ω_{av} approaches 180°.

Xanthine Oxidases. There are two types of EPR signals displayed by the two [2Fe−2S*] centers in the molybdenum (Mo) enzymes of the XO family. A first class of signals ("signal I") seems to fit quite well with the original B−G model.[13] This is, however, not the case for the set of "signal II", with the g_{max} component being as high as 2.16 in one case. Moreover, there is an overall shift of the three $\{g_i\}$ values toward larger values (the average *g* values range from 1.96 to 2.01).

Among the two [2Fe−2S*] clusters that are present in this XO family, the *distal* cluster relative to the Mo active site belongs to class A, whereas the *proximal* cluster belongs to class B (see Figure 9). The attribution of the EPR spectra to each of the two 2Fe centers has long been the object of a great debate,[40−44,59,60] which has been recently resolved in favor of signal I being assigned to the proximal cluster.[13]

We computed (with much effort because of the lack of symmetry) the complete **g** tensors for $[2Fe-2S^*](SH)_4$ by modeling the proximal (nonplant-type class B) centers for two systems based on the aldehyde oxidoreductase (PDF ID: 1HLR[69]) and on the carbon monoxide dehydrogenase (PDB ID: 1FFV[70]) geometries. These two systems correspond experimentally to the two extremes in terms of the (signal II) g_{max} values. As in all of our previous calculations, we did not include the effects of the hydrogen bonds and (putative) exogeneous nearby molecules, and the ferric **g** tensor was again taken as isotropic (2.02). The computed *g* values correspond to those typically found for class A type systems, and we do not see for the moment what could increase g_{max} to values as large as 2.16.

Conclusion

Our DFT calculations on the reduced $[2Fe-2S](SH)_4$ clusters led us to predict the existence of a good correlation between the principal *g* values and the well-defined structural ligand feature Ω_{av} for the representatives of class A. The angle, an average of the two Fe−Fe−S−C_β(Cys) dihedral angles Ω_1 and Ω_2 on the ferrous side, characterizes a large class of proteins for which $\Omega_1 \approx \Omega_2$ (C_2 symmetry). The B−G phenomenological parameter θ, which mixes a $d_{x^2-y^2}$ component into the supposedly mainly ferrous ground-state d_{z^2} orbital, is replaced here by the structural angle Ω_{av}. Moreover, for the experimental values of Ω_{av} (120−150°), the d_{xy} ferrous d orbital turns out to compete with the d_{z^2} (d_{z^2} is the main contributor only around 0° and 180° within the C_2 symmetry). This radically changes the analysis of the **g**, magnetic hyperfine, and quadrupole tensors, especially their principal vectors. We are aware that, from a strictly experimental point of view, Figure 10 has been drawn with dihedral angles extracted from the oxidized protein structures. This prediction for the *reduced* systems will have to be validated as more crystal structures are determined for the reduced [2Fe−2S*] systems.

Finally, the correlation between the **g** principal values (and principal vectors) and actual structural angles allows the prediction of the fine structural features around the ferrous site (axial tensor for lower, and rhombic tensor for higher, Ω_{av} angle values). Reciprocally, such a correlation establishes Ω_{av} as the main parameter for the determination of the **g** tensors before other possible candidates, such as the number of hydrogen bonds, the deformation of the [2Fe−2S*] core, etc.

The PDB ID's are as follows: 1FXI[61] (ferredoxin (fdx) I from the blue-green alga *Aphanothece sacrum* at 2.2 Å), 1GAQ[62] (complex between fdx and fdx−$Nadp^+$ reductase at 2.59 Å), 1FRR[63] (fdx I from *Equisetum arvense* at 1.8 Å), 1A70[55] (fdx I from *Spinacia oleracea* at 1.7 Å), 1DOI[64] (fdx from *Haloarcula marismortui* at 1.9 Å), 1FO4[65] (bovine milk xanthine dehydrogenase at 2.1 Å), 1AWD[66] (fdx from *Chlorella fusca* at 1.4 Å), 1FIQ[65] (bovine milk xanthine oxidase at 2.5 Å), 1J7A,B,C[67] (fdx from *Anabaena* at 1.8 Å), 1CZP[43] (fdx from *Anabaena* at 1.17 Å), 1KRH[68]

(58) Fukuyama, K.; Ueki, N.; Nakamura, H.; Tsukihara, T.; Matsubara, H. *J. Biochem.* **1995**, *117*, 1017.
(59) Romao, M. J.; Knäblein, J.; Huber, R.; Moura, J. J. G. *Prog. Biophys. Mol. Biol.* **1997**, *68*, 121−144.
(60) Lowe, D. J.; Mitchell, C. J.; Bray, R. C. *Biochem. Soc. Trans.* **1997**, *25*, 527S.
(61) Tsukihara, T.; Fukuyama, K.; Mizushima, M.; Harioka, T.; Kusunoki, M.; Katsube, Y.; Hase, T.; Matsubara, H. *J. Mol. Biol.* **1990**, *216*, 399.
(62) Kurisu, G.; Kusunoki, M.; Katoh, E.; Yamazaki, T.; Teshima, K.; Onda, Y.; Kimita-Ariga, Y.; Hase, T. *Nat. Struct. Biol.* **2001**, *8*, 117.
(63) Ikemizu, S.; Bando, M.; Sato, T.; Morimoto, Y.; Tsukihara, T.; Fukuyama, K. *Acta Crystallogr., Sect. D: Biol. Crystallogr.* **1994**, *50*, 167.
(64) Frolow, F.; Harel, M.; Sussman, J. L.; Mevarech, M.; Shoham, M. *Nat. Struct. Biol.* **1996**, *3*, 452.
(65) Enroth, C.; Eger, B. T.; Okamoto, K.; Nishino, T.; Nishino, T.; Pai, E. F. *Proc. Natl. Acad. Sci. U.S.A.* **2000**, *97*, 10723.
(66) Bes, M. T.; Parisini, E.; Inda, L. A.; Saraiva, L. M.; Peleato, M. L.; Sheldrick, G. M. *Structure* **1999**, *7*, 1201.
(67) Hurley, J. K.; Weber-Main, A. M.; Stankovich, M. T.; Benning, M. M.; Thoden, J. B.; Vanhooke, J. L.; Holden, H. M.; Chae, Y. K.; Xia, B.; Cheng, H.; Markley, J. L.; Martinez-Julvez, M.; Gómez-Moreno, C.; Schmeits, J. L.; Tollen, G. *Biochemistry* **1997**, *36*, 11100−11117.
(68) Karlsson, A.; Beharry, Z. M.; Eby, D. M.; Coulter, E. D.; Niedle, E. L.; Jr., D. M. K.; Eklund, H.; Ramaswamy, S. *J. Mol. Biol.* **2002**, *318*, 503.

(benzoate 1,2-dioxygenase from *Acinetobacter* at 1.5 Å), 1HLR[69] (aldehyde oxidoreductase from *Desulfovibrio gigas*), 1FFV[70] (carbon monoxide dehydrogenase with Mo from *Hydrogenophaga pseudoflava* at 2.25 Å), 1FFU[70] (carbon monoxide dehydrogenase without Mo at 2.35 Å), 1QLA[71] (fumarate reductase from *Wolinella succinogenes* at 2.2 Å), 1QJ2[72] (Co dehydrogenase from *Oligotropha carboxidovorans* at 1.5 Å), 1EP1[73] (dihydroorotate dehydrogenase B from *Lactococcus lactis* at 2.2 Å), 2PIA[74] (phthalate dioxygenase reductase from *Burkholderia cepacia* at 2.0 Å), 1I7H[75] (adrenodoxin-type fdx from *Escherichia coli* at 1.7 Å), 1AYF[52] (bovine adrenodoxin at 1.85 Å), 1L5P[76] (fdx from *Trichomonas vaginalis* at 2.2 Å), 1E6E[77] (fdx from *Rhodobacter capsulatus* at 2.07 Å), 1E9M[78] (fdx from *Rhodobacter capsulatus* at 2.07 Å), 1M2A[79] (fdx from *Aquifex aelolicus* at 1.5 Å: from an electronic point of view, the proteins characterized by the Ω angles around −120° are indistinguishable from those of the main group with the Ω set around +120°), 1HRK[80] (human ferrochelatase at 2.0 Å).

Acknowledgment. We gratefully thank Jacques Meyer (DRDC-BECP, CEA—Grenoble), Marc Fontecave (DRDC-CBCRB, CEA—Grenoble), and Juan Carlos Fontecilla-Camps (LCCP, IBS—Grenoble) for their helpful discussions.

Supporting Information Available: Mathematical expressions of the **g**, the dipolar magnetic hyperfine, and the quadrupole tensors in the case of C_2 symmetry. Also provided is the contour plot of the d_{z^2} contribution (%) to the sixth d ferrous orbital (Figure S1) as well as the contour plot of the HOMO−LUMO (d−d) gap (Figure S2), as a function of the two Fe−Fe−S−H dihedral angles for the $[2Fe-2S^*](SH)_4$ model. This material is available free of charge via the Internet at http://pubs.acs.org.

IC0301167

(69) Rebelo, J. M.; Dias, J. M.; Huber, R.; Moura, J. J.; Romao, M. J. *J. Biol. Inorg. Chem.* **2001**, *6*, 791.
(70) Haenzelmann, P.; Dobbek, H.; Gremer, L.; Huber, R.; Meyer, O. *J. Mol. Biol.* **2000**, *301*, 1223.
(71) Lancaster, C. R. D.; Kroeger, A.; Auer, M.; Michel, H. *Nature* **1999**, *402*, 377.
(72) Dobbek, H.; Gremer, L.; Kiefersauer, R.; Huber, R.; Meyer, O. *Proc. Natl. Acad. Sci. U.S.A.* **2002**, *99*, 15971.
(73) Rowland, P.; Norager, S.; Jensen, K. F.; Larsen, S. *Structure* **2000**, *8*, 1227.
(74) Correll, C. C.; Batie, C. J.; Ballou, D. P.; Ludwig, M. L. *Science* **1992**, *258*, 1604.
(75) Katuka, Y.; Horio, T.; Takahashi, Y.; Fukuyama, K. *Biochemistry* **2001**, *40*.
(76) Crossnoe, C. R.; Germanas, J. P.; LeMagueres, P.; Mustata, G.; Krause, K. L. *J. Mol. Biol.* **2002**, *318*, 503.
(77) Mueller, J. J.; Lapko, A.; Bourenkov, G.; Ruckpaul, K.; Heinemann, U. *J. Biol. Chem.* **2001**, *276*, 2786.
(78) Armengaud, J.; Sainz, G.; Jouanneau, Y.; Sieker, L. C. *Acta Crystallogr., Sect. D: Biol. Crystallogr.* **2001**, *57*, 301.
(79) Yeh, A. P.; Ambroggio, X. I.; Andrade, S. L. A.; Einsle, O.; Chatelet, C.; Meyer, J.; Rees, D. C. *J. Biol. Chem.* **2002**, *277*, 34499.
(80) Wu, C. K.; Dailey, H. A.; Rose, J. P.; Burden, A.; Sellers, V. M.; Wang, B. C. *Nat. Struct. Biol.* **2000**, *8*, 156.
(81) Bray, R. C.; George, N.; Lange, R.; Meyer, O. *Biochem. J.* **1983**, *211*, 687−694.
(82) Knoell, H.; Knappe, J. *Eur. J. Biochem.* **1974**, *50*, 245−252.
(83) Vidakovic, M. S.; Fraczkiewicz, G.; Germanas, J. P. *J. Biol. Chem.* **1996**, *271*, 14734−14739.
(84) Naud, I.; Vinçon, M.; Garin, J.; Gaillard, J.; Forest, E.; Jouanneau, Y. *Eur. J. Biochem.* **1994**, *222*, 933−939.